ADVANCED ENERGY MATERIALS
www.advenergymat.de

3D Printing of Tunable Energy Storage Devices with Both High Areal and Volumetric Energy Densities

Tingting Gao, Zhan Zhou, Jianyong Yu, Jing Zhao, Guiling Wang, Dianxue Cao, Bin Ding, and Yiju Li**

Developing advanced supercapacitors with both high areal and volumetric energy densities remains challenging. In this work, self-supported, compact carbon composite electrodes are designed with tunable thickness using 3D printing technology for high-energy-density supercapacitors. The 3D carbon composite electrodes are composed of the closely stacked and aligned active carbon/carbon nanotube/reduced graphene oxide (AC/CNT/rGO) composite filaments. The AC microparticles are uniformly embedded in the wrinkled CNT/rGO conductive networks without using polymer binders, which contributes to the formation of abundant open and hierarchical pores. The 3D-printed ultrathick AC/CNT/rGO composite electrode (ten layers) features high areal and volumetric mass loadings of 56.9 mg cm^{-2} and 256.3 mg cm^{-3}, respectively. The symmetric cell assembled with the 3D-printed thin GO separator and ultrathick AC/CNT/rGO electrodes can possess both high areal and volumetric capacitances of 4.56 F cm^{-2} and 10.28 F cm^{-3}, respectively. Correspondingly, the assembled ultrathick and compact symmetric cell achieves high areal and volumetric energy densities of 0.63 mWh cm^{-2} and 1.43 mWh cm^{-3}, respectively. The all-component extrusion-based 3D printing offers a promising strategy for the fabrication of multiscale and multidimensional structures of various high-energy-density electrochemical energy storage devices.

1. Introduction

Supercapacitors, as a typical electrochemical energy storage device, have attracted extensive attention owing to the high power density, favorable charge/discharge reversibility, long cycle stability, and excellent reliability.[1–3] However, the relatively low energy density of supercapacitors severely hampers their further development and widespread practical applications. As the core components of supercapacitors, the electrode materials play a determined role in offering high performance for supercapacitors. There are usually two ways to enhance the electrochemical performance of supercapacitors. One is exploring new electrode materials with high surface area and conductivity, such as advanced carbon-based materials, and the other one is constructing reasonable electrode structure with unimpeded electron and ion pathways.[4–8] To date, many efforts have been dedicated to developing a variety of carbonaceous materials with different morphologies, such as CNT, AC, graphene, carbon nanofibers, whereas less attention has been focused on the optimization of carbon-based electrode structures.[9–13] How to properly design and regulate the electrode microstructures (electrode architecture engineering) based on the existed materials using advanced fabrication and assembly methods to further optimize the performance is also of great significance.

A few fabrication and assembly methods, such as vacuum filtration,[14] freeze-casting,[15] solvothermal gelation,[16] and chemical vapor deposition (CVD),[17] have been proposed to adjust the carbon-based electrode architectures. However, for the CVD method, it is expensive and not scalable, and the obtained electrode structures are generally fragile. The electrode architecture prepared by the vacuum filtration, freeze-casting and solvothermal gelation is largely stochastic and highly tortuous, which greatly hinders electrolyte ion transport. Thus, the controllable and scalable electrode fabrication with tailored architectures remains a great challenge.[18] The extrusion-based

T. Gao, Prof. J. Yu, Prof. B. Ding
Key Laboratory of Textile Science & Technology
Ministry of Education, College of Textiles
Donghua University
Shanghai 201620, P. R. China
E-mail: yujy@dhu.edu.cn

Z. Zhou
College of Materials Science and Engineering
Donghua University
Shanghai 201620, P. R. China

The ORCID identification number(s) for the author(s) of this article can be found under https://doi.org/10.1002/aenm.201802578.

DOI: 10.1002/aenm.201802578

J. Zhao, Prof. G. Wang, Prof. D. Cao
Key Laboratory of Superlight Materials and Surface Technology
Ministry of Education
College of Materials Science and Chemical Engineering
Harbin Engineering University
Harbin 150001, P. R. China

Dr. Y. Li
Department of Materials Science and Engineering
College of Engineering
Peking University
Beijing 100871, P. R. China
E-mail: liyijuliyiju2014@outlook.com, 1806391027@pku.edu.cn

© 2018 WILEY-VCH Verlag GmbH & Co. KGaA, Weinheim

3D printing, as one of the most facile and versatile additive manufacturing technologies, can directly print out multifarious delicate and complex structures in a low-cost, adjustable and scalable way. The printing strategy and architecture design of the extrusion-based 3D printing are highly related with the rheological properties of ink materials.[19] Due to the rich amphiphiles, stable dispersion capability and tunable rheological behavior, the graphene oxide (GO) is commonly selected to formulate multiple aqueous composite inks for extrusion-based 3D printing.[20] The rheological properties of the GO-based inks can be manipulated by adjusting the concentration of the ink and additives for different printing purposes, such as tuning formability, porosity, conductivity, and stability. Currently, diverse GO-based electrode structures including mesh, interdigitation and microlattice structures have been successfully constructed via the extrusion-based 3D printing.[21–23] However, these electrode architectures are not compact, and most of these 3D electrodes maintain low mass loading to ensure enough ion transport paths and high active material utilization. It follows that high gravimetric capacitance is usually obtained at the sacrifice of areal and volumetric capacitances. Nevertheless, in some practical applications, especially for the compact energy storage, high energy storage capacity within the specified area or volume is the top priority. As a result, constructing compact, thick and high-mass-loading 3D electrodes with fast electron and ion transport to achieve high areal and volumetric capacitances is of great importance.

In this work, we designed self-supported thin GO separator and compact brick-like active carbon/carbon nanotube/reduced graphene oxide (AC/CNT/rGO) carbon composite electrodes with tunable thickness using the layer-by-layer extrusion-based 3D printing technology for high-energy-density supercapacitors. The 3D-printed carbon composite electrodes are composed of the closely stacked and aligned AC/CNT/rGO composite filaments. The 3D AC microparticles with high surface area serve as the active materials, 1D CNTs are interconnected with each other to form conductive networks. The 2D rGO nanosheets serve as binder and support to adhere and accommodate the AC microparticles. The reasonable assembly of various multidimensional carbon materials (from 1D to 3D) within the 3D-printed, compact electrodes contributes to the formation of abundant open and hierarchical pores (from microscale to nanoscale), which can offer pathways for electrolyte ion diffusion. As a result, the 3D-printed ultrathick AC/CNT/rGO composite electrode (ten layers) with both high areal and volumetric mass loadings of 56.9 mg cm^{-2} and 256.3 mg cm^{-3}, respectively, can feature high areal and volumetric capacitances of 9.16 F cm^{-2} and 41.3 F cm^{-3}, respectively. The assembled symmetric supercapacitor based on the 3D-printed thin GO separator and ultrathick AC/CNT/rGO electrodes can possess high areal and volumetric capacitances of 4.56 F cm^{-2} and 10.28 F cm^{-3}, respectively. In addition, the areal and volumetric energy densities of the ultrathick symmetric cell can reach 0.63 mWh cm^{-2} and 1.43 mWh cm^{-3}, respectively. Our work demonstrates that the layer-by-layer extrusion-based 3D printing is a promising strategy for customized high-energy-density electrode fabrication in the energy-storage-related fields.

2. Results and Discussion

Figure 1a briefly shows the ink preparation and 3D printing process of the electrode and separator. The AC/CNT/GO composite ink for electrode preparation was formulated by simply mixing AC, CNT, and GO precursor suspension (20 mg mL^{-1}) in a certain weight proportion to create a uniformly dispersed and high-viscosity composite ink. The GO precursor suspension can be directly concentrated through evaporation to form a homogeneous and low-viscosity GO ink for separator fabrication. The prepared AC/CNT/GO and GO inks were then separately loaded into two syringes attached with different grade metal needles for extrusion-based 3D printing. The designed patterns were directly printed out on a flat substrate through a program-controlled 3D printer. To fabricate the AC/CNT/rGO composite electrodes, the AC/CNT/GO composite ink was printed to fine filaments with a line spacing of 0.25 mm and an in-plane zigzag layout (1 cm × 1 cm) to construct a multilayer, closely stacked monolithic structure in a layer-by-layer 3D printing manner (Video S1, Supporting Information), followed by drying and carbonization. The GO separator was built by directly writing the GO ink on a hydrophilic polyvinylidene fluoride (PVDF) membrane with a line spacing of 0.4 mm through a rectangle cycle printing manner (Video S2, Supporting Information). The 3D-printed GO film can be processed into a self-standing thin separator through drying and low-temperature stabilization.

The properties of printed structures are strongly dependent on the rheological properties of inks in the extrusion-based 3D printing process. A printable ink for extrusion-based 3D printing should exhibit typical shear-thinning behavior and a sufficient zero shear viscosity to ensure good extrudability of the slurry and favorable shape maintenance of the printed filament.[24] Since the rheology properties are mainly determined by the concentrations of the GO-based inks, the concentrations of the prepared inks need to be carefully controlled to tailor their respective rheological behaviors. To print compact and thick electrode structure, the concentration of the AC/CNT/GO ink was controlled to be as high as 350 mg mL^{-1}. For the GO separator fabrication, the concentration of the GO ink was optimized to be 30 mg mL^{-1} (Figure S1, Supporting Information). The detailed evaluations of rheology properties of these two inks were investigated under ambient temperature. Figure 1b shows the viscosity as a function of the shear rate on a log scale for the AC/CNT/GO and GO inks. Both inks demonstrate a strong shear-thinning behavior, wherein the apparent viscosity decreases at the high shear rate, suggesting the inks could flow through a fine nozzle under extruding. The AC/CNT/GO ink with a high concentration exhibits a higher viscosity over the shear rate range compared to the GO ink with a low concentration. It is also found that the viscosity tends to infinity around the low shear-rate, which indicates the inks behave as a Bingham plastic with yield stress. The Bingham plastic behavior is a result of the addition of GO suspension, making the ink return to a zero-shear condition and retain the filament shape once the applied stress is removed.[25]

The yield stress can be estimated by applying an oscillatory stress sweep to inks at a frequency of 1 Hz. Figure 1c displays the curves of the storage modulus (G') and loss modulus (G'')

© 2018 WILEY-VCH Verlag GmbH & Co. KGaA, Weinheim

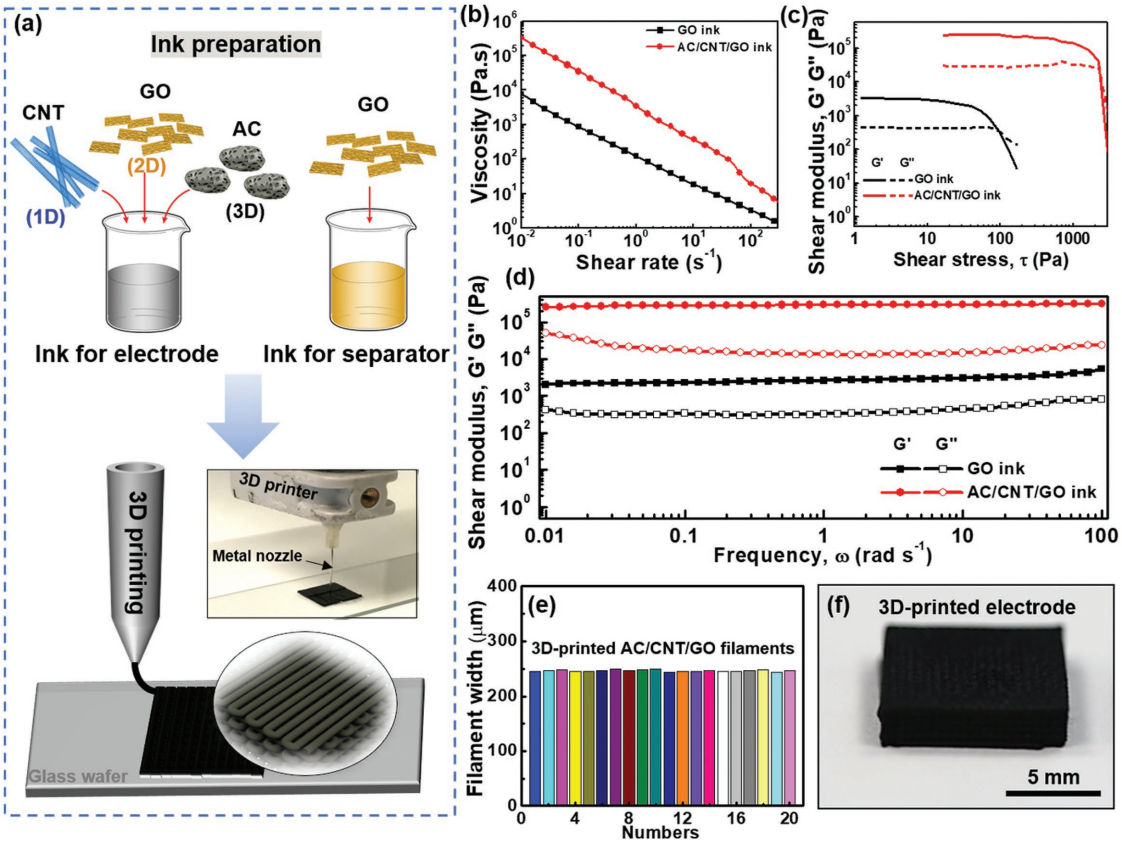

Figure 1. 3D printing process and rheological properties of inks. a) Schematic showing the fabrication of the 3D-printed carbon composite electrode and separator. b) Apparent viscosity as a function of shear rate for the GO and AC/CNT/GO inks. c) Storage modulus (G′) and loss modulus (G″) as a function of shear stress for the GO and AC/CNT/GO inks. Both inks display yielding behavior and typical viscoelastic properties. d) Dynamic modulus (G′ and G″) as a function of frequency for the GO and AC/CNT/GO inks. The stable values of G′ and G″ at different frequencies demonstrate the superior rheological stability of the GO and AC/CNT/GO inks. e) Width variation of the 3D-printed AC/CNT/GO filaments. f) Photograph showing the 3D-printed thick carbon composite electrode (ten layers).

as a function of stress amplitude. It can be observed that two inks with different viscosities exhibit different yield stress. The yield stress (τ_y) of the AC/CNT/GO and GO inks is ≈1700 and 50 Pa, respectively. Below the flow point ($G' > G''$), both inks display a typical elastic-like solid with the G' tending to keeping constant at low shear stress. Upon yielding, the G' of both inks drops sharply and eventually surpasses the G'', indicating the transition from solid to liquid behaviors. It should be noticed that the G′ and G″ of the AC/CNT/GO ink are much higher than those of the GO ink, where the plateau values of G' are about 320 000 and 3200 Pa for the AC/CNT/GO and GO inks, respectively. The higher G' indicates a stiffer character of the AC/CNT/GO ink, which is desirable for printing self-supported complex structures without deformation.[26]

Figure 1d shows the shear modulus of the AC/CNT/GO and GO inks as a function of frequency. The oscillatory frequency sweeps of the AC/CNT/GO and GO inks both display that the G' is larger than G″ within the entire frequency interval tested, indicating that both inks exhibit the viscoelastic behavior with typical gel at rest.[27] In addition, the frequency-independent modulus suggests a 3D network of force existed within the inks, which enables long-term dispersion stability in static state.[21] We further investigated the width variation of the 3D-printed compactly arranged AC/CNT/GO filaments (Figure 1e). The narrow width variation demonstrates the relatively high printed structural accuracy. The results of the rheological analysis demonstrate the favorable printability of the AC/CNT/GO and GO inks for the extrusion-based 3D printing. The fidelity of the inks after printing was also qualitatively judged by digital photos. Figure S2a–c (Supporting Information) shows the digital photos of the printed AC/CNT/GO and GO inks on the glass substrate at an incline of 50°. It can be found that the AC/CNT/GO ink with a high viscosity remains a stereoscopic structure at different angles. The phenomenon reveals that the AC/CNT/GO ink is able to create favorable structural features that can retain the printed shape immediately and support themselves without collapse after printing (Figure 1f). For the printed GO ink with a low viscosity, it tends to merge with itself and even slightly deforms at an oblique angle of 50°. Actually, due to the favorable spreadability of the GO ink, it is in favor of generating a thin, homogenous, and self-standing film, of which some adjacent filaments can be merged together (Figure S3, Supporting Information).

After drying and annealing, the customized 3D AC/CNT/rGO composite architectures were obtained, which can be directly used as the electrodes for energy storage device. The

© 2018 WILEY-VCH Verlag GmbH & Co. KGaA, Weinheim

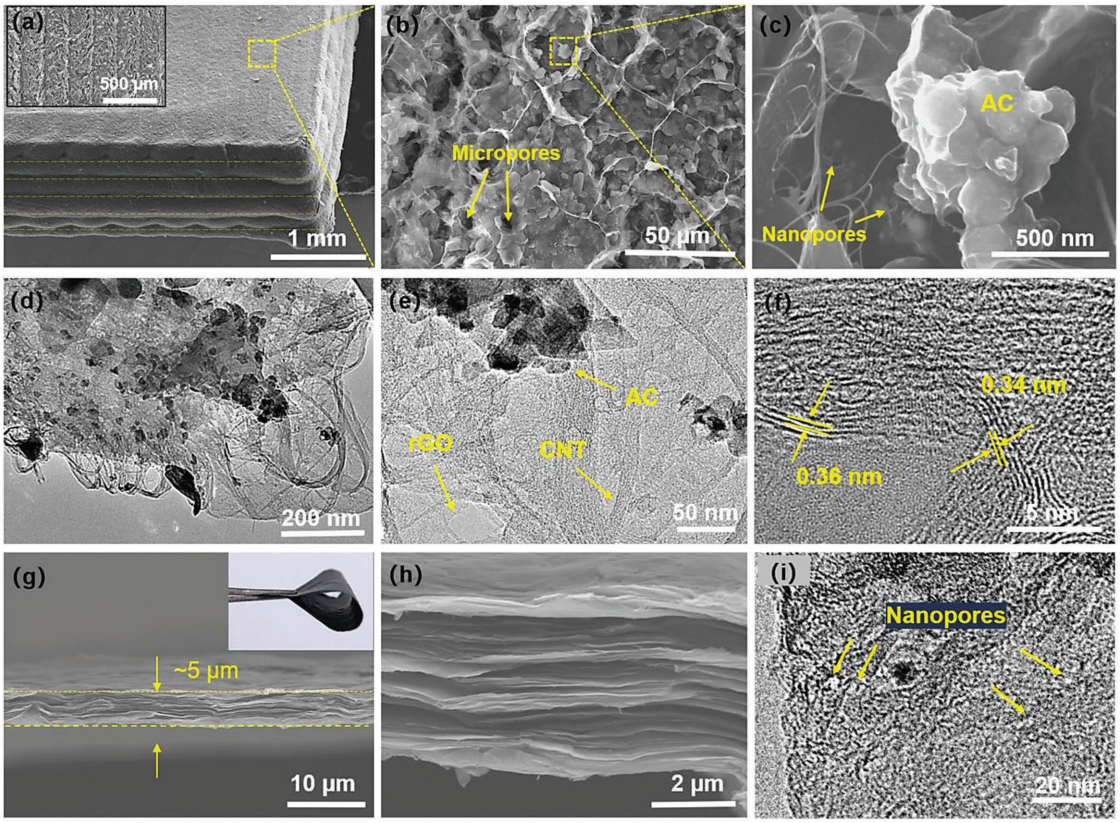

Figure 2. Morphologies of the 3D-printed carbon composite electrode and separator. a) SEM image showing the lateral view of the 3D-printed AC/CNT/rGO composite electrode. Inset showing the top surface of electrode, where the AC/CNT/rGO filaments stack closely. b,c) Zoomed-in SEM images of the 3D-printed AC/CNT/rGO composite electrode. AC microparticles are uniformly distributed across the CNT/rGO network. d,e) TEM images of the 3D-printed AC/CNT/rGO composite. The AC particles tightly anchor on the interconnected CNT/rGO substrate. f) HRTEM image of the 3D-printed AC/CNT/rGO composite electrode. The lattice fringe distances of 0.34 and 0.36 nm are probably attributed to the (002) crystal planes of the CNT and rGO, respectively. g) SEM image showing the thickness of the 3D-printed GO separator (thickness: 5 µm). Inset in Figure 2g demonstrates the favorable flexibility of the GO separator. h) SEM image of the cross section of the GO separator, which is assembled with GO sheets in a layer-by-layer manner. i) TEM image of the single GO nanosheet with abundant in-plane nanopores.

detailed microstructure of the 3D-printed AC/CNT/rGO electrodes was investigated using scanning electron microscopy (SEM) and transmission electron microscopy (TEM). **Figure 2**a shows the lateral view of the 3D-printed AC/CNT/rGO composite electrode. The multilayer AC/CNT/rGO composite electrode is composed of continuous and zig-zag filaments, which are stacked tightly (inset in Figure 2a). The structure stability of the AC/CNT/rGO composite electrode was investigated by the press test under a weight of 200 g (Figure S4, Supporting Information). There are no obvious filament fracture and collapse after the press test, which indicates excellent structure stability. The enlarged SEM images reveal that the AC microparticles are densely and uniformly embedded in the 3D CNT/rGO networks without apparent aggregation (Figure 2b,c). Especially, it can be observed that there are abundant hierarchical pores in the 3D-printed AC/CNT/rGO electrode, of which the pore size is distributed from several micrometers to dozens of nanometers. The 3D-printed compact AC/CNT/rGO composite electrode with hierarchically porous structure allows sufficient electrolyte infiltration and facilitates fast ion diffusion. The inner microstructure of the 3D-printed AC/CNT/rGO composite electrode is revealed in Figure S5a–c (Supporting Information). The 3D wrinkled CNT/rGO frameworks compactly accommodate numerous AC microparticles. As clearly illustrated in Figure S5d, numerous CNTs conformally covered on the rGO sheets are interconnected with each other to form a spiderweb-like network, which construct fast electron transport pathways.

The microstructure of the 3D-printed AC/CNT/rGO composite electrode was further investigated by TEM. As displayed in Figure 2d,e, the irregular AC particles are anchored on the rGO/CNT networks. The lattice fringes with distances of 0.34 and 0.36 nm can be observed in the high-resolution TEM (HRTEM) image, which are possibly attributed to the (002) crystal planes of the CNT and rGO, respectively (Figure 2f). The thin GO separator can be rapidly fabricated by the extrusion-based 3D printing process and easily peeled off from the substrate after low-temperature stabilization. As shown in Figure 2g, the obtained GO membrane with a thickness of 5 µm is free-standing and flexible. Due to the shear flow condition during the 3D printing process, the GO sheets with high aspect ratio are well aligned along the extruding direction and assembled into a multilamellar structure (Figure 2h). The abundant in-plane nanopores and capillary channels formed in the interlayers of the GO membrane allow ions to transport quickly

© 2018 WILEY-VCH Verlag GmbH & Co. KGaA, Weinheim

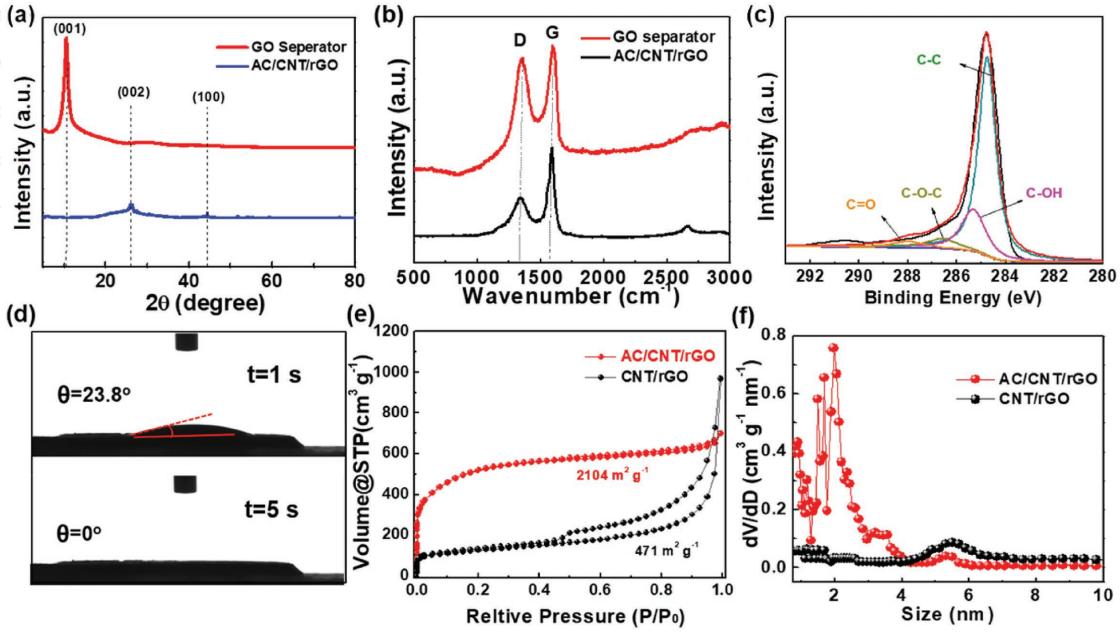

Figure 3. Characterizations of the 3D-printed AC/CNT/rGO composite electrode and GO separator. a) XRD patterns of the 3D-printed GO separator and AC/CNT/rGO composite electrode. b) Raman spectra of the 3D-printed GO separator and AC/CNT/rGO composite electrode. c) High-resolution C1s XPS spectrum of the 3D-printed AC/CNT/rGO composite electrode. d) Contact angle test of the 3D-printed AC/CNT/rGO composite electrode (ten layers). The electrolyte droplet can be totally absorbed into the electrode within 5 s. e) BET adsorption/desorption isotherms of the 3D-printed AC/CNT/rGO and CNT/rGO composite electrodes (ten layers). f) Size distributions of the 3D-printed AC/CNT/rGO and CNT/rGO composite electrodes.

through the hydrated GO membrane (Figure 2i). In addition, the gaps between the adjacent GO filaments can further facilitate fast ion transport across the GO membrane (Figure S6, Supporting Information).

Figure 3a shows the X-ray diffraction (XRD) patterns of the 3D-printed GO separator and AC/CNT/rGO composite electrode. For the GO separator, the sharp diffraction peak located at 10.6° corresponds to the (001) crystal plane of GO.[28] Based on the Bragg's law, the interlayer distance between the GO sheets is estimated to be 0.834 nm, which is much larger than that of the pristine graphite (0.34 nm). Two broad diffraction peaks located at 25.9° and 44.3° for the 3D-printed AC/CNT/rGO composite electrode are attributed to the (002) and (100) planes diffractions of carbon materials, respectively.[29] Raman analysis was carried out to investigate the graphitic feature of the carbon samples (Figure 3b). The peaks at ≈1350 and ≈1580 cm^{-1} are assigned to the D and G bands, respectively. The integral intensity ratio of G to D peaks (I_G/I_D) is commonly used to evaluate the graphitic degree of carbon.[30] The low I_G/I_D value of the GO separator (0.52) suggests a highly amorphous feature and an inferior degree of order, which is consistent with the XRD result. The I_G/I_D value of the AC/CNT/rGO composite electrode is about 1.3, indicating high graphitization level. Moreover, the appearance of a 2D peak at ≈2650 cm^{-1} also suggests the high level of graphitic ordering. The high graphitization degree indicates the high electronic conductivity of the 3D-printed AC/CNT/rGO composite electrode, which contributes to enhancing the electrochemical performance, especially at high charge/discharge current densities. Moreover, we further investigated the electrical conductivity of the 3D-printed AC/CNT/rGO-*X* composite electrodes with different layers (*X* represents layer; *X* = 1, 2, 4, and 10) based on the direct current (DC) ohmic measurements. The 3D-printed AC/CNT/rGO-1, 2, 4, and 10 composite electrodes exhibit a high electrical conductivity of 3.18, 2.82, 2.58, and 2.4 S m^{-1}, respectively (Figure S7, Supporting Information).

To investigate the surface chemical composition of the 3D-printed AC/CNT/rGO composite, X-ray photoelectron spectroscopy (XPS) analysis was conducted. Figure 3c shows the high-resolution XPS spectrum of C 1s. The deconvoluted C 1s XPS spectrum reveals that the surface of AC/CNT/rGO composite is primarily dominated by the C—C bond (sp^2 and sp^3 C) (284.7 eV). The peaks located at 285.4, 286.6, and 288.1 eV are assigned to the C—OH, C—O—C and C = O species, respectively.[31] The relatively high contents of oxygenic functional groups suggest the favorable hydrophilicity of the 3D-printed AC/CNT/rGO composite electrode. To further confirm the excellent electrolyte wettability of the 3D-printed AC/CNT/rGO composite electrode and GO separator, we conducted the wetting angle measurements. As shown in Figure 3d and Figure S8 (Supporting Information), the contact angles of the electrolyte droplet on the surface of the AC/CNT/rGO composite electrode and GO separator are about 23.8° and 60° after 1 s, respectively, and the electrolyte droplet can be rapidly absorbed into the electrode within 5 s. The small initial contact angle and the short wetting time manifest an excellent wettability of the 3D-printed AC/CNT/rGO composite electrode, enabling fast electrolyte penetration into the electrode microstructure. Besides the porosity, conductivity, and wettability, the specific surface area and size distribution of electrode also play a significant role in the optimization of electrochemical performance. Figure 3e displays the Brunauer–Emmett–Teller (BET) adsorption/desorption isotherms of the

© 2018 WILEY-VCH Verlag GmbH & Co. KGaA, Weinheim

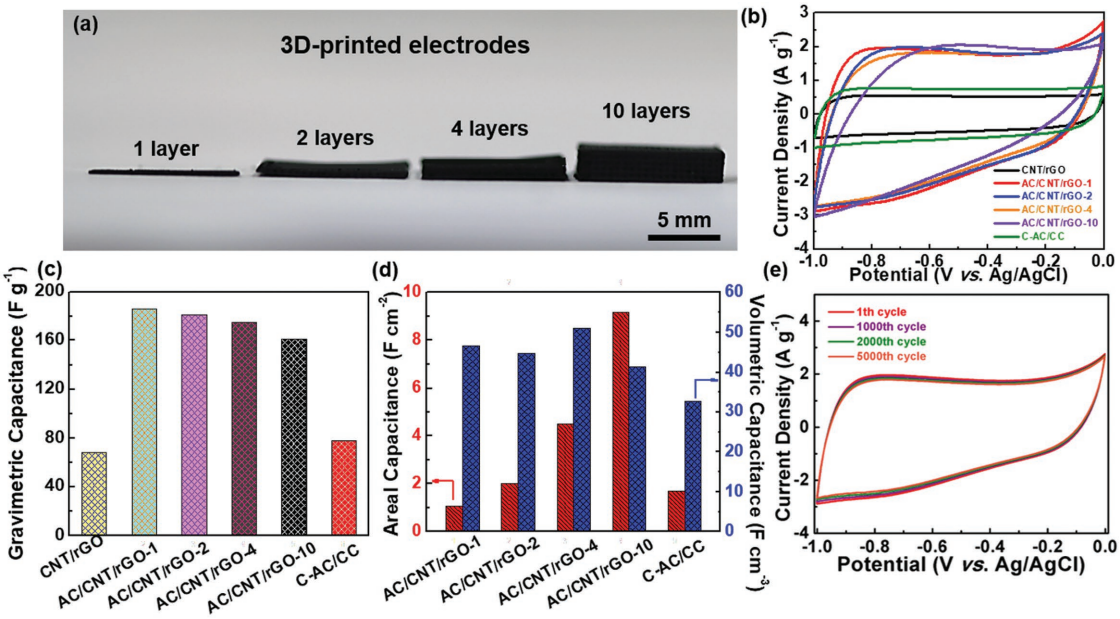

Figure 4. Electrochemical performance of the 3D-printed carbon composite electrodes and conventional slurry-based electrode. a) Photograph showing the thickness of the 3D-printed AC/CNT/rGO composite electrodes with different layers (1, 2, 4, and 10 layers). b) CV curves of the 3D-printed CNT/rGO, AC/CNT/rGO-1, AC/CNT/rGO-2, AC/CNT/rGO-4, AC/CNT/rGO-10, and C-AC/CC electrodes at a scan rate of 10 mV s^{-1}. c) Comparison of the gravimetric capacitance of various electrodes at a scan rate of 10 mV s^{-1} (based on the entitle weight of electrode). d) Comparison of the areal and volumetric capacitances of various electrodes at a scan rate of 10 mV s^{-1}. e) Cycling performance of the 3D-printed AC/CNT/rGO-1 composite electrode after different cycles (scan rate: 10 mV s^{-1}).

3D-printed AC/CNT/rGO and CNT/rGO (without adding AC) composite electrodes (ten layers). For the 3D-printed AC/CNT/rGO composite, the rapid increase of adsorbed volume at the initial relative pressure (P/P_o) suggests the existence of abundant micropores and small mesopores, which are mainly originated from the AC microparticles.[32] Additionally, the broad knee in the low P/P_o range and well-defined plateaus of adsorbed volume further indicate the existence of numerous mesopores and micropores.[33] For the 3D-printed CNT/rGO composite, the obvious H_3 hysteresis loop demonstrates the inferior pore openness and rough pore wall owing to the GO stacking.[34] The pore size distribution of carbon specimens derived from the adsorption branch of the isotherm was calculated according to the density functional theory (DFT) model (Figure 3f). The pore size of the 3D-printed AC/CNT/rGO composite is mainly distributed at 0.8, 1.7, 1.8, 2.1, 3.2, and 5.4 nm. As a contrast, the pore size of the CNT/rGO composite is focused at 5.5 nm, lacking abundant hierarchical micropores and mesopores.

Figure 4a shows the photographs of the 3D-printed AC/CNT/rGO-X composite electrodes with different thicknesses. The electrode thickness increases with the increase of the 3D-printed layers. For comparison, the conventional slurry-based electrode was also prepared by coating the slurry of commercial AC, carbon black, and PVDF on a carbon cloth (CC) and was denoted as the C-AC/CC. The thickness of the entire C-AC/CC electrode is about 500 µm (Figure S9, Supporting Information). To investigate the electrochemical performance of various electrodes, we tested the CV curves at a scan rate of 10 mV s^{-1} in a three-electrode system. As shown in Figure 4b, the area of CV curves of the C-AC/CC and 3D-printed CNT/rGO electrodes is much smaller than that of 3D-printed AC/CNT/rGO-X composite electrodes, which indicates the relatively lower gravimetric capacitance of the C-AC/CC and 3D-printed CNT/rGO electrodes. The gravimetric capacitance of a thick electrode is usually supposed to be inferior due to the extended ion and electron transport pathways. However, for the 3D-printed ultrathick AC/CNT/rGO-10 composite electrode, its gravimetric capacitance can still reach 161 F g^{-1} at a scan rate of 10 mV s^{-1}, which is comparable with those of the 3D-printed AC/CNT/rGO-1 (186 F g^{-1}), AC/CNT/rGO-2 (181 F g^{-1}), and AC/CNT/rGO-4 (175 F g^{-1}) composite electrodes, and much higher than those of the CNT/rGO (68 F g^{-1}) and C-AC/CC (78 F g^{-1}) electrodes (Figure 4c). The rate performance of various electrodes was summarized in Figure S10 (Supporting Information). The gravimetric capacitance retentions of the 3D-printed AC/CNT/rGO-1, 2, 4, and 10 composite electrodes are 81%, 79%, 77%, and 72% from the scan rate of 5–100 mV s^{-1}, respectively, which are higher than that of the conventional C-AC/CC electrode (56.7%). The favorable rate performance of the 3D-printed AC/CNT/rGO-X composite electrodes could be attributed to the open and hierarchically porous microstructure. The interconnected CNTs not only act as electron transport pathways, but also serve as the spacers to prevent the stack of rGO nanosheets, offering numerous unimpeded electrolyte ion channels. Additionally, the conformal and plicated rGO networks are 3D hosts for homogenously and compactly accommodating the active materials of AC without using polymer binders.

The gravimetric capacitance is commonly used to indicate the number of active sites per unit weight and tends to obtain a high value under a low mass loading. In fact, the capacitances

© 2018 WILEY-VCH Verlag GmbH & Co. KGaA, Weinheim

under specific area and volume are also significant parameters to evaluate the electrochemical performance of energy storage devices, especially in the applications of compact energy storage. A higher electrode thickness usually generates a higher areal capacitance (Figure S11, Supporting Information). As shown in Figure 4d, the areal capacitances of the 3D-printed AC/CNT/rGO-X electrodes increase with the increase of printed layers, and the 3D-printed AC/CNT/rGO-10 composite electrode can reach 9.16 F cm^{-2} at a scan rate of 10 mV s^{-1}, which is much superior to the C-AC/CC electrode (1.68 F cm^{-2}). Moreover, when considering the electrode thickness, the volumetric capacitances of the 3D-printed AC/CNT/rGO-X electrodes are still higher than those of the C-AC/CC electrode (Figure S12, Supporting Information). The 3D-printed AC/CNT/rGO-10 composite electrode shows a volumetric capacitance of 41.3 F cm^{-3} at a scan rate of 10 mV s^{-1}, much higher than that of the C-AC/CC electrode (32.8 F cm^{-3}) (Figure 4d). The ultrathick and compact AC/CNT/rGO-10 composite electrode with both high areal and volumetric capacitances is attributed to the open and hierarchical microstructure enabled by the extrusion-based 3D printing technology. The cycling performance of the 3D-printed carbon composite electrodes was further investigated using the accelerated CV measurement. It can be observed from Figure 4e, the shape of CV curves of the 3D-printed AC/CNT/rGO-1 electrode remains almost the same after different cycles, which demonstrates excellent long-term cycling stability.

We further investigated the electrochemical performance of the symmetric supercapacitors assembled with two same AC/CNT/rGO-X electrodes and a GO separator (**Figure 5**a).

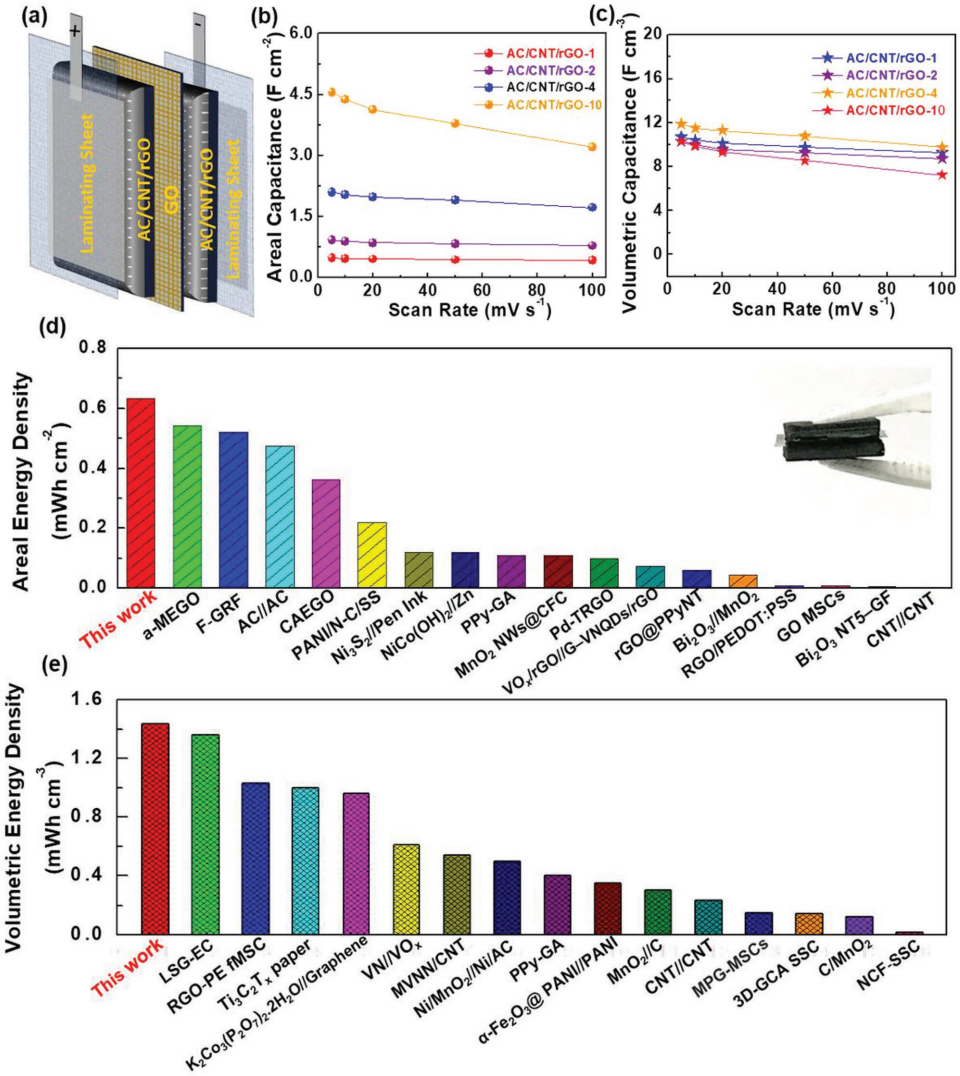

Figure 5. Electrochemical performance of the assembled AC/CNT/rGO symmetric supercapacitors. a) Schematic showing the assembled structure of the AC/CNT/rGO symmetric supercapacitor. b) Comparison of the areal capacitance of various 3D-printed AC/CNT/rGO symmetric supercapacitors with different electrode thicknesses. c) Comparison of the volumetric capacitance of various 3D-printed AC/CNT/rGO symmetric capacitors with different electrode thicknesses. d) Comparison of the areal energy density of our 3D-printed AC/CNT/rGO-10 symmetric supercapacitor with the other symmetric/asymmetric capacitors. e) Comparison of the volumetric energy density of our 3D-printed AC/CNT/rGO-10 symmetric supercapacitor with the other symmetric/asymmetric capacitors.

© 2018 WILEY-VCH Verlag GmbH & Co. KGaA, Weinheim

Figure S13 (Supporting Information) shows the CV curves of the AC/CNT/rGO-X symmetric supercapacitors at scan rates from 5 to 100 mV s^{-1}. It can be observed that the area of CV curves of the AC/CNT/rGO-X symmetric supercapacitors under same scan rate gradually decreases with the increase of electrode layers, indicating the decrease of gravimetric capacitance. Moreover, the shape distortion of the rectangular-like CV curves of the AC/CNT/rGO-X symmetric supercapacitors becomes more severe with the increase of electrode layers. The result demonstrates the thicker AC/CNT/rGO-X electrodes suffer from relatively slower electrochemical kinetics, which could result from the extended electron and ion pathways. The result is also confirmed by the electrochemical impedance spectroscopy (EIS) measurement. As shown in Figure S14 (Supporting Information), the combined series (R_s, the intercept at Re(Z)-axis, related to the internal resistance of the system) and charge transfer resistances (R_{ct}, the diameter of semicircle, related to the redox reaction kinetics of oxygenic functional groups on carbon) increase with the increase of electrode thickness. The linear curves in the low frequency region are related with the ion diffusion process. The larger slope of the curves indicates the smaller ion diffusion resistance.[35] It is clear that the thicker supercapacitor suffers from higher ion diffusion resistance. The tortuosity of the 3D-printed AC/CNT/rGO electrodes with different thicknesses was further investigated to evaluate the effect of the electrode structure on the effective electrolyte ion transport properties. The tortuosity values of the 3D-printed AC/CNT/rGO-1, 2, 4, 10 electrodes can be estimated to be about 1.58, 1.63, 1.76, and 1.83, respectively (Tortuosity Measurement section in the Supporting Information; Figure S15). The tortuosity increases with the electrode thickness, which is consistent with the EIS results. It should be noted that, even for the ultrathick AC/CNT/rGO-10 electrode, its tortuosity is much lower than those of the slurry-coated electrodes (3–30).[36] The low tortuosity of the 3D-printed AC/CNT/rGO electrodes contributes to the unimpeded electrolyte ion transport. The gravimetric capacitance of the AC/CNT/rGO-X symmetric supercapacitors versus scan rate is shown in Figure S16 (Supporting Information). The gravimetric capacitances of the 3D-printed AC/CNT/rGO-1, 2, 4, and 10 symmetric supercapacitors are 42.7, 42.3, 41.0, and 40.2 F g^{-1}, respectively, at a scan rate of 5 mV s^{-1}. Even at a high scan rate of 100 mV s^{-1}, the gravimetric capacitances of the 3D-printed AC/CNT/rGO-1, 2, 4, and 10 symmetric supercapacitors can still reach 37.2, 36.0, 33.6, and 27.4 F g^{-1}, respectively.

The areal capacitances of the 3D-printed AC/CNT/rGO-1, 2, 4, and 10 symmetric supercapacitors under various scan rates are displayed in Figure 5b. The areal capacitance of the 3D-printed ultrathick AC/CNT/rGO-10 symmetric supercapacitor can reach 4.56 F cm^{-2}, which is almost ten times larger than that of the AC/CNT/rGO-1 symmetric supercapacitor (0.48 F cm^{-2}). We further calculated the volumetric capacitance of the AC/CNT/rGO-1, 2, 4, and 10 symmetric supercapacitors at different scan rates, and the results are displayed in Figure 5c. All AC/CNT/rGO-X symmetric supercapacitors exhibit relatively high volumetric capacitances (10.70, 10.30, 11.88, and 10.28 F cm^{-3} for the 3D-printed AC/CNT/rGO-1, 2, 4, and 10 symmetric supercapacitors, respectively, at a scan rate of 5 mV s^{-1}), which are attributed to the densely assembled macroarchitecture and hierarchical microstructure enabled by the extrusion-based layer-by-layer 3D printing. As a comparison, we also prepared film-casted AC/CNT/rGO electrodes and investigated the electrochemical performance of the symmetric cell assembled with the film-casted AC/CNT/rGO electrodes. As shown in Figure S17a,b (Supporting Information), the film-casted AC/CNT/rGO composite film with a thickness of 205 μm is smooth and dense. We compared the electrochemical performance of the symmetric cells assembled with the 3D-printed AC/CNT/rGO-1 and film-casted AC/CNT/rGO electrodes owing to the similar electrode thickness. The CV curves of the symmetric cells assembled with the 3D-printed AC/CNT/rGO-1 and film-casted AC/CNT/rGO electrodes at 10 mV s^{-1} are shown in Figure S17c (Supporting Information). The area of CV curve of the 3D-printed AC/CNT/rGO-1 symmetric cell is larger than that of the symmetric cell assembled with the film-casted AC/CNT/rGO electrodes, which indicates the relatively larger gravimetric capacitance of the 3D-printed AC/CNT/rGO-1 symmetric cell. The calculated gravimetric, areal and volumetric capacitances of the symmetric cell assembled with the film-casted AC/CNT/rGO electrodes are 21.6 F g^{-1}, 0.37 F cm^{-2}, and 9.1 F cm^{-3}, respectively, which are lower than those of the 3D-printed AC/CNT/rGO-1 symmetric cell (Figure S17d, Supporting Information). The inferior electrochemical performance of the symmetric cell assembled with the film-casted AC/CNT/rGO electrodes could be attributed to the hampered mass transfer resulted from the tortuous and less porous electrode structure.

The cycling performance of the 3D-printed AC/CNT/rGO-1, 2, 4, and 10 symmetric cells was further investigated. The specific capacitance retentions of the AC/CNT/rGO-1, 2, 4, and 10 symmetric supercapacitors remain 98.2%, 97.8%, 94.3% and 93.3% after 5000 cycles, respectively, indicating superior cycling stability (Figure S18, Supporting Information). The microstructure of the 3D-printed AC/CNT/rGO-10 electrode after cycling test was revealed in Figure S19a,b (Supporting Information). There is no obvious structure collapse, and the filaments remain the hierarchical structure after the cycling test, which indicate the excellent structure stability. The gravimetric, areal and volumetric energy densities of the 3D-printed AC/CNT/rGO-1, 2, 4, and 10 symmetric supercapacitors as a function of scan rate were summarized in Figures S20–S22 (Supporting Information). In general, our assembled ultrathick AC/CNT/rGO-10 symmetric supercapacitor can deliver a maximum areal energy density of 0.63 mWh cm^{-2}, which compares favorably with many advanced energy storage devices, such as a-MEGO,[37] F-GRF,[38] CAEGO,[39] PANI/N-C/SS,[40] Ni_3S_2//Pen Ink,[41] $NiCo(OH)_2$//Zn,[42] GO MSCs,[22] PPy-GA,[23] MnO_2 NWs@CFC,[43] rGO@PPyNT,[44] Bi_2O_3//MnO_2,[45] RGO/PEDOT:PSS,[46] Bi_2O_3 NT5-GF,[47] VO_x/rGO//G–VNQDs/rGO,[26] CNT//CNT,[48] Pd-TRGO,[49] and AC//AC symmetric/asymmetric cells (Figure 5d).[50] Meanwhile, benefiting from the compact electrode architecture and abundant hierarchical pores, the volumetric energy density of the 3D-printed ultrathick AC/CNT/rGO-10 symmetric supercapacitor can reach 1.43 mWh cm^{-3}, which is superior than those recently reported supercapacitors, such as CNT//CNT,[48] LSG-EC,[51] $Ti_3C_2T_x$ paper,[52] VN//VO_x,[53] MVNN/CNT,[54] Ni/MnO_2//Ni/AC,[55] α-Fe_2O_3@PANI//PANI,[56] MnO_2//C,[57] MPG-MSCs,[58] C/MnO_2,[59] 3D-GCA

© 2018 WILEY-VCH Verlag GmbH & Co. KGaA, Weinheim

SSC,[18] PPy-GA,[23] NCF-SSC,[60] $K_2Co_3(P_2O_7)_2 \cdot 2H_2O$//Graphene,[61] and GRO-PE fMSC cells.[62] The results corroborate that the extrusion-based 3D-printing offers a promising electrode architecture engineering strategy for achieving high-energy-density energy storage devices.

3. Conclusion

In this work, we used the extrusion-based 3D printing to construct ultrathick and compact all-GO-based supercapacitors with both high areal and volumetric energy densities. The 3D-printed carbon composite electrodes with tunable thickness are composed of closely stacked AC/CNT/rGO filaments. The wrinkled rGO sheets decorated with interconnected CNT networks serve as 3D hosts for conformally and densely accommodating the active materials of AC without using polymer binders. The self-supported compact AC/CNT/rGO electrodes with open and hierarchical pores possess both fast electron and ion transport pathways, which can enhance the electrochemical performance including capacitance and rate capability. As a result, the symmetric supercapacitor assembled with the 3D-printed thin GO separator and ultrathick AC/CNT/rGO-10 electrodes has high areal and volumetric capacitances of 4.56 F cm^{-2}, and 10.28 F cm^{-3}, respectively. Especially, the assembled AC/CNT/rGO-10 symmetric cell possesses high areal and volumetric energy densities of 0.63 mWh cm^{-2} and 1.43 mWh cm^{-3}, respectively. This work offers a high-efficiency manufacturing approach to constructing reasonable electrode architectures for various advanced high-energy-density electrochemical energy storage devices.

Supporting Information

Supporting Information is available from the Wiley Online Library or from the author.

Acknowledgements

The authors acknowledge the support of the National Natural Science Foundation of China (51572052) and Initiative Postdocs Supporting Program (BX20180001). Y.L. designed the experiments. Y.L. and T.G. conducted the experiments. T.G. and Y.L. conducted rheology tests and provided the rheology analysis. Z.Z. and Y.L. created the 3D illustrations. Y.L., J.Z., D.C., G.W., and B.D. provided characterizations (XRD, SEM, TEM, XPS, BET, and Raman). Y.L., T.G., and J.Y. wrote the paper. All authors commented on the final manuscript.

Conflict of Interest

The authors declare no conflict of interest.

Keywords

3D printing, carbon, high energy density, symmetric supercapacitors, tunable

Received: August 19, 2018
Revised: October 27, 2018
Published online:

[1] Z. Yu, L. Tetard, L. Zhai, J. Thomas, *Energy Environ. Sci.* **2015**, *8*, 702.
[2] G. Wang, L. Zhang, J. Zhang, *Chem. Soc. Rev.* **2012**, *41*, 797.
[3] C. Liu, F. Li, L. P. Ma, H. M. Cheng, *Adv. Mater.* **2010**, *22*, E28.
[4] B. G. Choi, M. Yang, W. H. Hong, J. W. Choi, Y. S. Huh, *ACS Nano* **2012**, *6*, 4020.
[5] L. Hao, X. Li, L. Zhi, *Adv. Mater.* **2013**, *25*, 3899.
[6] L. Yu, H. Hu, H. B. Wu, X. W. Lou, *Adv. Mater.* **2017**, *29*, 1604563.
[7] X. Feng, Y. Liang, L. Zhi, A. Thomas, D. Wu, I. Lieberwirth, U. Kolb, K. Müllen, *Adv. Funct. Mater.* **2009**, *19*, 2125.
[8] M. Yu, S. Zhao, H. Feng, L. Hu, X. Zhang, Y. Zeng, Y. Tong, X. Lu, *ACS Energy Lett.* **2017**, *2*, 1862.
[9] Y. Cheng, S. Lu, H. Zhang, C. V. Varanasi, J. Liu, *Nano Lett.* **2012**, *12*, 4206.
[10] Y. Xia, T. S. Mathis, M.-Q. Zhao, B. Anasori, A. Dang, Z. Zhou, H. Cho, Y. Gogotsi, S. Yang, *Nature* **2018**, *557*, 409.
[11] S. Xu, G. Wei, J. Li, W. Han, Y. Gogotsi, *J. Mater. Chem. A* **2017**, *5*, 17442.
[12] S. L. Candelaria, Y. Shao, W. Zhou, X. Li, J. Xiao, J.-G. Zhang, Y. Wang, J. Liu, J. Li, G. Cao, *Nano Energy* **2012**, *1*, 195.
[13] G. Xu, C. Zheng, Q. Zhang, J. Huang, M. Zhao, J. Nie, X. Wang, F. Wei, *Nano Res.* **2011**, *4*, 870.
[14] J. Du, C. Zheng, W. Lv, Y. Deng, Z. Pan, F. Kang, Q.-H. Yang, *Adv. Mater. Interfaces* **2017**, *4*, 1700004.
[15] Y. Shao, M. F. El-Kady, C. W. Lin, G. Zhu, K. L. Marsh, J. Y. Hwang, Q. Zhang, Y. Li, H. Wang, R. B. Kaner, *Adv. Mater.* **2016**, *28*, 6719.
[16] Y. Xu, K. Sheng, C. Li, G. Shi, *ACS Nano* **2010**, *4*, 4324.
[17] Z. Chen, W. Ren, L. Gao, B. Liu, S. Pei, H.-M. Cheng, *Nat. Mater.* **2011**, *10*, 424.
[18] C. Zhu, T. Liu, F. Qian, T. Y.-J. Han, E. B. Duoss, J. D. Kuntz, C. M. Spadaccini, M. A. Worsley, Y. Li, *Nano Lett.* **2016**, *16*, 3448.
[19] T. Jungst, W. Smolan, K. Schacht, T. Scheibel, J. Groll, *Chem. Rev.* **2016**, *116*, 1496.
[20] E. García-Tuñón, E. Feilden, H. Zheng, E. D'Elia, A. Leong, E. Saiz, *ACS Appl. Mater. Interfaces* **2017**, *9*, 32977.
[21] S. D. Lacey, D. J. Kirsch, Y. Li, J. T. Morgenstern, B. C. Zarket, Y. Yao, J. Dai, L. Q. Garcia, B. Liu, T. Gao, *Adv. Mater.* **2018**, *30*, 1705651.
[22] W. Li, Y. Li, M. Su, B. An, J. Liu, D. Su, L. Li, F. Li, Y. Song, *J. Mater. Chem. A* **2017**, *5*, 16281.
[23] Z. Qi, J. Ye, W. Chen, J. Biener, E. B. Duoss, C. M. Spadaccini, M. A. Worsley, C. Zhu, *Adv. Mater. Technol.* **2018**, *3*, 1800053.
[24] N. Paxton, W. Smolan, T. Böck, F. Melchels, J. Groll, T. Jungst, *Biofabrication* **2017**, *9*, 044107.
[25] D. W. McOwen, S. Xu, Y. Gong, Y. Wen, G. L. Godbey, J. E. Gritton, T. R. Hamann, J. Dai, G. T. Hitz, L. Hu, *Adv. Mater.* **2018**, *30*, 1707132.
[26] K. Shen, J. Ding, S. Yang, *Adv. Energy Mater. 8*, **2018**, 1800408.
[27] K. Shen, H. Mei, B. Li, J. Ding, S. Yang, *Adv. Energy Mater.* **2018**, *8*, 1701527.
[28] Y. Zhao, W. Ran, J. He, Y. Huang, Z. Liu, W. Liu, Y. Tang, L. Zhang, D. Gao, F. Gao, *Small* **2015**, *11*, 1310.
[29] X. Dong, H. Jin, R. Wang, J. Zhang, X. Feng, C. Yan, S. Chen, S. Wang, J. Wang, J. Lu, *Adv. Energy Mater.* **2018**, *8*, 1702695.
[30] H. Li, Y. Tao, X. Zheng, J. Luo, F. Kang, H.-M. Cheng, Q.-H. Yang, *Energy Environ. Sci.* **2016**, *9*, 3135.
[31] Y. Li, D. Cao, Y. Wang, S. Yang, D. Zhang, K. Ye, K. Cheng, J. Yin, G. Wang, Y. Xu, *J. Power Sources* **2015**, *279*, 138.
[32] J. Zhao, H. Lai, Z. Lyu, Y. Jiang, K. Xie, X. Wang, Q. Wu, L. Yang, Z. Jin, Y. Ma, *Adv. Mater.* **2015**, *27*, 3541.
[33] P. K. Tripathi, M. Liu, Y. Zhao, X. Ma, L. Gan, O. Noonan, C. Yu, *J. Mater. Chem. A* **2014**, *2*, 8534.
[34] Y. Li, G. Wang, T. Wei, Z. Fan, P. Yan, *Nano Energy* **2016**, *19*, 165.
[35] T. S. Wei, B. Y. Ahn, J. Grotto, J. A. Lewis, *Adv. Mater.* **2018**, *30*, 1703027.
[36] I. V. Thorat, D. E. Stephenson, N. A. Zacharias, K. Zaghib, J. N. Harb, D. R. Wheeler, *J. Power Sources* **2009**, *188*, 592.

 © 2018 WILEY-VCH Verlag GmbH & Co. KGaA, Weinheim

[37] S. Murali, N. Quarles, L. L. Zhang, J. R. Potts, Z. Tan, Y. Lu, Y. Zhu, R. S. Ruoff, *Nano Energy* **2013**, *2*, 764.
[38] L. Sheng, J. Chang, L. Jiang, Z. Jiang, Z. Liu, T. Wei, Z. Fan, *Adv. Funct. Mater.* **2018**, *28*, 1800597.
[39] Y. Zhu, S. Murali, M. D. Stoller, K. Ganesh, W. Cai, P. J. Ferreira, A. Pirkle, R. M. Wallace, K. A. Cychosz, M. Thommes, *Science* **2011**, *332*, 1537.
[40] J. Cao, T. Huang, R. Liu, X. Xi, D. Wu, *Electrochim. Acta* **2017**, *230*, 265.
[41] J. Wen, S. Li, K. Zhou, Z. Song, B. Li, Z. Chen, T. Chen, Y. Guo, G. Fang, *J. Power Sources* **2016**, *324*, 325.
[42] Y. Huang, W. S. Ip, Y. Y. Lau, J. Sun, J. Zeng, N. S. S. Yeung, W. S. Ng, H. Li, Z. Pei, Q. Xue, *ACS Nano* **2017**, *11*, 8953.
[43] C. Hong, X. Wang, H. Yu, H. Wu, J. Wang, A. Liu, *Funct. Mater. Lett.* **2018**, *11*, 1850034.
[44] C. Yang, L. Zhang, N. Hu, Z. Yang, H. Wei, Y. Zhang, *J. Power Sources* **2016**, *302*, 39.
[45] H. Xu, X. Hu, H. Yang, Y. Sun, C. Hu, Y. Huang, *Adv. Energy Mater.* **2015**, *5*, 1401882.
[46] L. Kou, T. Huang, B. Zheng, Y. Han, X. Zhao, K. Gopalsamy, H. Sun, C. Gao, *Nat. Commun.* **2014**, *5*, 3754.
[47] K. Gopalsamy, Z. Xu, B. Zheng, T. Huang, L. Kou, X. Zhao, C. Gao, *Nanoscale* **2014**, *6*, 8595.
[48] W. Yu, H. Zhou, B. Q. Li, S. Ding, *ACS Appl. Mater. Interfaces* **2017**, *9*, 4597.
[49] A. Azhari, E. Marzbanrad, D. Yilman, E. Toyserkani, M. A. Pope, *Carbon* **2017**, *119*, 257.
[50] M. Areir, Y. Xu, D. Harrison, J. Fyson, *Mater. Sci. Eng. B* **2017**, *226*, 29.
[51] M. F. El-Kady, V. Strong, S. Dubin, R. B. Kaner, *Science* **2012**, *335*, 1326.
[52] M. R. Lukatskaya, O. Mashtalir, C. E. Ren, Y. Dall'Agnese, P. Rozier, P. L. Taberna, M. Naguib, P. Simon, M. W. Barsoum, Y. Gogotsi, *Science* **2013**, *341*, 1502.
[53] X. Lu, M. Yu, T. Zhai, G. Wang, S. Xie, T. Liu, C. Liang, Y. Tong, Y. Li, *Nano Lett.* **2013**, *13*, 2628.
[54] X. Xiao, X. Peng, H. Jin, T. Li, C. Zhang, B. Gao, B. Hu, K. Huo, J. Zhou, *Adv. Mater.* **2013**, *25*, 5091.
[55] L. Zhang, P. Zhu, F. Zhou, W. Zeng, H. Su, G. Li, J. Gao, R. Sun, C.-p. Wong, *ACS Nano* **2016**, *10*, 1273.
[56] X.-F. Lu, X.-Y. Chen, W. Zhou, Y.-X. Tong, G.-R. Li, *ACS Appl. Mater. Interfaces* **2015**, *7*, 14843.
[57] X. Lu, M. Yu, G. Wang, T. Zhai, S. Xie, Y. Ling, Y. Tong, Y. Li, *Adv. Mater.* **2013**, *25*, 267.
[58] Z. S. Wu, K. Parvez, X. Feng, K. Müllen, *Nat. Commun.* **2013**, *4*, 2487.
[59] X. Xiao, T. Li, P. Yang, Y. Gao, H. Jin, W. Ni, W. Zhan, X. Zhang, Y. Cao, J. Zhong, *ACS Nano* **2012**, *6*, 9200.
[60] K. Xiao, L.-X. Ding, G. Liu, H. Chen, S. Wang, H. Wang, *Adv. Mater.* **2016**, *28*, 5997.
[61] H. Pang, Y. Zhang, W.-Y. Lai, Z. Hu, W. Huang, *Nano Energy* **2015**, *15*, 303.
[62] Y. Liu, B. Zhang, Q. Xu, Y. Hou, S. Seyedin, S. Qin, G. G. Wallace, S. Beirne, J. M. Razal, J. Chen, *Adv. Funct. Mater.* **2018**, *28*, 1706592.

© 2018 WILEY-VCH Verlag GmbH & Co. KGaA, Weinheim